Applied Science and Engineering Progress, Vol. 20, No. 3, 2027, 8277

Research Article

The Influence of Fiber Orientation on the Energy Absorption Performance of Hybrid Double Hat Structures under Bending Impact

Worachat Senakum
Graduate Student, Department of Mechanical Engineering, Faculty of Industry and Technology, Rajamangala University of Technology Isan Sakon Nakhon Campus, Thailand

Kunanon Sakkampang* and Nirut Onsalung
Department of Mechanical Engineering, Faculty of Industry and Technology, Rajamangala University of Technology Isan Sakon Nakhon Campus, Thailand
The Material's Impact Resistance Testing Research Laboratory (Mat-Pact Lab), Faculty of Industry and Technology, Rajamangala University of Technology Isan Sakon Nakhon Campus, Thailand

* Corresponding author. E-mail: kunanon.sa@rmuti.ac.th DOI: 10.14416/j.asep.2026.08.019
Received: 27 March 2026; Revised: 18 May 2026; Accepted: 2 July 2026 ; Published online: 31 August 2026

Abstract
This study investigated the energy absorption performance of hybrid composite double hat structures made from carbon fiber reinforced polymer (CFRP) and glass fiber reinforced polymer (GFRP) under bending impact loading. Sixteen laminate configurations were fabricated using two stacking sequences, [0/90] and [45/−45], through a vacuum forming process. The specimens were tested using a vertical impact testing machine at an impact velocity of 5.42 m/s, and a finite element model was developed to simulate damage behavior under impact. The results showed that the carbon fiber configuration CC$[45/-45]_4$ achieved the highest specific energy absorption of 0.364 kJ/kg. Among the hybrid laminates, CG$[45/-45]_4$ achieved a specific energy absorption of 0.261 kJ/kg, demonstrating comparable performance with reduced material cost. These findings indicate that hybrid CFRP/GFRP composites can provide a cost-effective alternative for lightweight energy-absorbing structures without substantially compromising mechanical performance.

Keywords: Double hat structure, Energy absorption, Hybrid materials, Specific energy absorption

1 Introduction

In recent years, research on automotive body structures has increasingly focused on reducing thickness and weight to improve fuel efficiency. Traditional steel has progressively been replaced by advanced lightweight materials [1]-[3]. In addition to weight reduction, impact resistance and energy absorption remain important design requirements [4], [5]. Composite materials have therefore gained wide attention because of their high strength-to-weight ratio [6], high stiffness [7], [8], corrosion and wear resistance [9], light weight [10], energy absorption capability, and fatigue and thermal insulation performance [11], [12]. These materials consist mainly of a matrix and reinforcement, with fibers arranged in woven or layered configurations, resulting in improved mechanical strength [13]-[15]. Owing to these advantages, composites have been widely used in aerospace [16], [17], automotive [18]–[20], and construction applications [21], [22].

Recent studies have shown growing interest in hybrid composites, which combine more than one type of fiber to achieve specific mechanical and economic advantages [23]-[25]. Hybridization can reduce dependence on high-cost fibers while maintaining desirable structural performance. In particular, hybrid CFRP/GFRP laminates can reduce material cost while providing acceptable energy absorption. Previous studies have also shown that optimized stacking sequences and layer configurations can improve the impact resistance of hybrid composites [26], [27]. However, practical limitations should be carefully considered when selecting and combining different fiber types [28]. Further research is therefore needed to clarify the performance of hybrid composites for structural applications.

Composite materials are increasingly used in automotive structural components such as front bumpers [29], side bumpers [30], and protective components for electric vehicle battery systems [31]. Among these configurations, the double hat structure has attracted attention because of its application in the front and side regions of vehicle bodies [32]. The side region is particularly important because of its proximity to the passenger compartment and its exposure to bending-dominated impact loads during side collisions [33]. Previous studies have shown that material selection and structural thickness strongly affect crash performance under dynamic impact and quasi-static loading conditions [34], [35].

To examine laminate design under bending impact, the [0/90] and [45/−45] configurations were selected because they represent two fundamental load-transfer mechanisms. The [0/90] configuration forms an orthogonal square grid that resists axial and bending deformation, whereas the [45/−45] configuration creates a diamond-shaped grid that enhances shear load transfer. Other stacking sequences, such as quasi-isotropic, ±30°, and ±60° orientations, were not considered in order to isolate bending-dominated and shear-dominated responses under identical impact energy and improve the interpretability of the experimental and numerical results.

Dynamic impact loading is important because peak load and internal energy absorption are often higher than those observed in quasi-static tests [36]. Chen *et al.* [37] showed that hybrid CFRP/GFRP composite tubes provided higher crash resistance than single-fiber composites while reducing production cost. Bidadi *et al.* [38] also reported that the number of composite layers directly affects energy absorption, and that hybrid configurations with a [45/−45] fiber orientation showed better specific energy absorption than other stacking angles.

The mechanical response of composite structures under bending impact differs from axial crushing and quasi-static loading. In axial crushing, the load is applied along the longitudinal axis, leading to progressive folding, fragmentation, and relatively stable energy absorption. In contrast, bending impact introduces combined bending moments and shear forces, resulting in asymmetric deformation, localized damage initiation, and non-uniform stress distribution. Dynamic bending impact also involves strain-rate effects that can increase peak load and alter failure mechanisms. These differences highlight the need to investigate bending impact separately because it provides insights that cannot be fully captured through axial or quasi-static testing.

Finite element analysis (FEA) is widely used to investigate crash behavior, damage progression, and energy absorption in composite structures [39]-[42]. When validated against experiments, previous studies have reported discrepancies between predicted and measured values, typically within 10% or less [41]. FEA is particularly useful for examining axial and bending crushing mechanisms in thin-walled components and identifying deformation and collapse modes that are difficult to observe through laboratory testing alone [42], [43]. However, most existing FEA studies focus on single-fiber composites, and many use fully clamped boundary conditions, which can increase local stiffness and suppress realistic deformation during bending impact. Therefore, further investigation of hybrid composites under more realistic boundary conditions is needed.

Recent advances in composite research have also explored alternative reinforcement strategies and predictive modeling techniques. Natural fiber-reinforced composites have shown promising mechanical behavior and energy absorption for lightweight applications [44]. Machine learning has been applied to predict mechanical properties and accelerate material design [45], while multiscale modeling has provided deeper insight into damage initiation and propagation in fiber-reinforced composites [46]. These developments show the growing integration of experimental, numerical, and data-driven approaches in composite research.

Recent studies further confirm the importance of hybrid and carbon fiber-reinforced composites for lightweight structural and crashworthiness applications. Techawinyutham *et al.* [47] investigated sustainable epoxy composites reinforced with hemp, pineapple, and glass fibers for lightweight automobile panels and showed that hybrid natural/synthetic fiber systems can improve mechanical and impact performance for semi-structural automotive applications. Kumar *et al.* [48] applied machine learning techniques to predict the bearing response of hydrothermally aged carbon fiber-reinforced epoxy composite joints, demonstrating the growing role of data-driven methods in evaluating composite performance under environmental degradation. Recent studies have also emphasized that CFRP composites are widely used because of their low density, high specific strength, fatigue resistance, and suitability for advanced engineering structures [49]. In addition, Kumar and Saini [50] compared different failure criteria for bidirectional carbon fiber/epoxy nanocomposites and reported that progressive damage analysis using criteria such as Hashin can support more reliable prediction of composite failure. These recent studies strengthen the relevance of the present work, which combines experimental bending impact testing and finite element analysis to evaluate hybrid CFRP/GFRP double hat structures for energy absorption applications.

Despite extensive research on composite structures, limited studies have examined the bending impact response of hybrid double hat configurations under realistic boundary conditions. Most previous investigations have focused on axial crushing behavior or simplified boundary constraints, which do not fully represent deformation in practical automotive applications. In addition, the influence of fiber orientation on the transition between bending-dominated and shear-dominated energy absorption mechanisms in hybrid laminates remains insufficiently explored.

Therefore, this study investigates the energy absorption performance of hybrid CFRP/GFRP double hat structures under bending impact loading using combined experimental and numerical validation. Unlike previous studies that mainly used fully clamped boundary conditions or single-fiber composite systems, this work adopts a free-support configuration to reproduce realistic bending-impact behavior and natural load transfer. The novelty of this study lies in correlating experimentally observed failure mechanisms with finite element predictions across different laminate configurations. Total energy absorption, specific energy absorption, and damage characteristics are systematically evaluated to support the design and manufacturing of lightweight automotive impact structures.

2 Materials and Methods

2.1 *Design principle of the double hat structure used in the test*

In this study, the test specimen was designed to represent a simplified structural component commonly used in automotive side structures. The geometry was based on the side region of a vehicle body, which typically consists of a rectangular section reinforced with extended flanges. When two hat-shaped components are positioned on the upper and lower sides of the section, the structure is referred to as a double hat configuration. Due to limitations of the impact testing system, the specimen was scaled down from actual automotive components while maintaining realistic geometric characteristics. Each specimen had a total length of 300 mm and a cross-sectional width of 60 mm. The upper and lower hat sections had a constant height

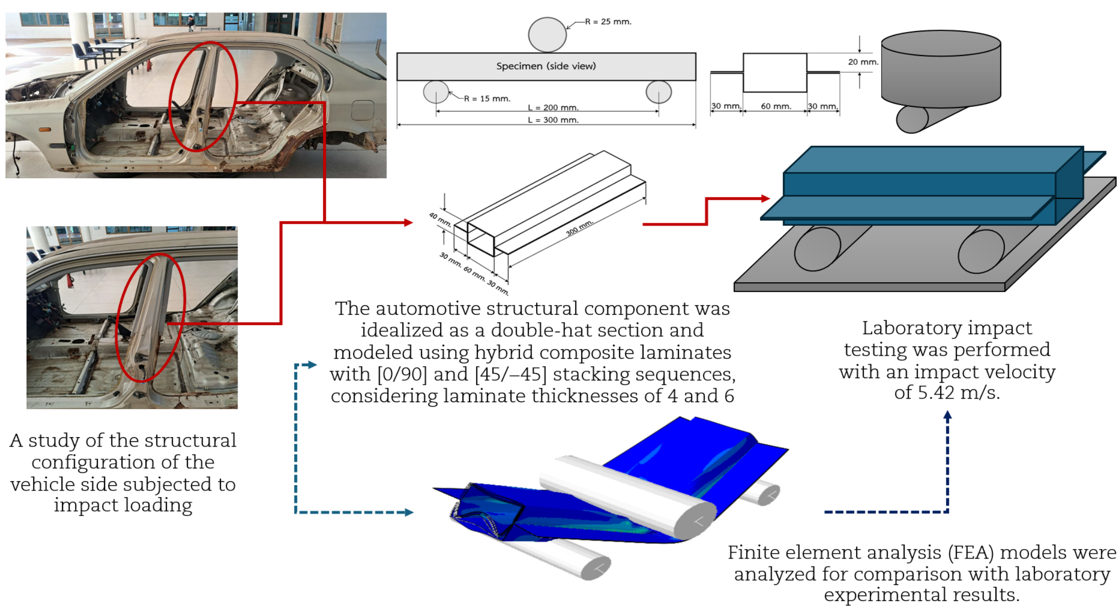

Figure 1: Dimensions of the double hat structure used in this study.

Applied Science and Engineering Progress, Vol. 20, No. 3, 2027, 8277

Table 1: Carbon and glass fiber stacking configurations used in this study.

No.	Layup sequence	Material	No. of layers	Laminate features
1	$CC[0/90]_4$	Carbon fiber	4	C[0/90]C[0/90]
2	$CC[45/-45]_4$	Carbon fiber	4	C[45/-45]C[45/-45]
3	$CCC[0/90]_6$	Carbon fiber	6	C[0/90]C[0/90]C[0/90]
4	$CCC[45/-45]_6$	Carbon fiber	6	C[45/-45]C[45/-45] C[45/-45]
5	$GG[0/90]_4$	Fiber glass	4	G[0/90]G[0/90]
6	$GG[45/-45]_4$	Fiber glass	4	G[45/-45]G[45/-45]
7	$GGG[0/90]_6$	Fiber glass	6	G[0/90]G[0/90]G[0/90]
8	$GGG[45/-45]_6$	Fiber glass	6	G[45/-45]G[45/-45] G[45/-45]
9	$CG[0/90]_4$	Carbon fiber/ Fiber glass	4	C[0/90]G[0/90]
10	$CG[45/-45]_4$	Carbon fiber/ Fiber glass	4	C[45/-45]G[45/-45]
11	$CGC[0/90]_6$	Carbon fiber/ Fiber glass	6	C[0/90]G[0/90]C[0/90]
12	$CGC[45/-45]_6$	Carbon fiber/ Fiber glass	6	C[45/-45]G[45/-45] C[45/-45]
13	$GC[0/90]_4$	Fiber glass/ Carbon fiber	4	G[0/90]C[0/90]
14	$GC[45/-45]_4$	Fiber glass/ Carbon fiber	4	G[45/-45]C[45/-45]
15	$GCG[0/90]_6$	Fiber glass/ Carbon fiber	6	G[0/90]C[0/90]G[0/90]
16	$GCG[45/-45]_6$	Fiber glass/ Carbon fiber	6	G[45/-45]C[45/-45] G[45/-45]

of 20 mm, with a flange width of 30 mm. The overall configuration is shown in Figure 1.

This study employed two composite materials widely used in automotive applications: unidirectional carbon fiber and glass fiber. These materials were laminated layer by layer to form the required structural configurations. Four fiber orientations, 0°, 90°, 45°, and −45°, were selected because they allow simple manufacturing and represent different load-transfer behaviors. The [0/90] and [45/−45] configurations represent bending-dominated and shear-dominated mechanisms, respectively. From a structural mechanics perspective, the [0/90] configuration forms an orthogonal square grid aligned with the longitudinal and transverse directions of the structure, which is effective in resisting bending deformation under impact. In contrast, the [45/−45] configuration forms a diamond-shaped grid that enhances shear load transfer and promotes shear-dominated deformation. For example, in the carbon [0/90] sequence, the first layer was oriented at 0° along the longitudinal axis of the specimen, followed by a second layer at 90° along the transverse axis. This stacking process was repeated to obtain the required configuration, as shown in Figure 2.

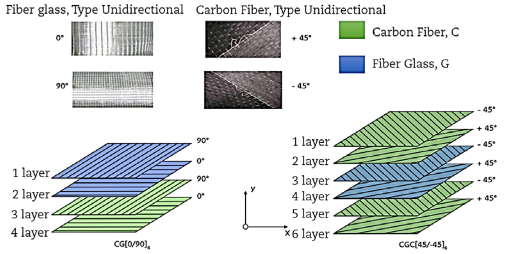

Figure 2: Fiber orientation patterns of carbon and glass fiber laminates used in the design.

Previous studies on hybrid and single-fiber composite structures have typically used between three and nine layers [46], [51]-[54]. Based on this range, the present study selected four-layer and six-layer specimens. This thickness range was considered suitable because, under the selected impact conditions and specimen size, collapse behavior and failure modes could be clearly observed.

Other stacking sequences, such as quasi-isotropic or intermediate angle-ply configurations, including ±30° and ±60°, were not considered in order to limit the number of design variables and enable a clear comparison between bending-dominated and shear-dominated responses under identical impact energy. Therefore, two main stacking styles were examined: the cross-ply configuration [0/90] and the angle-ply configuration [45/−45]. In total, sixteen stacking configurations were designed for the experiment, as summarized in Table 1.

The possible effect of laminate asymmetry and bending-twisting coupling was also considered in the selection of fiber orientations. In composite laminates, bending-twisting coupling can occur when the stacking sequence is unbalanced or highly asymmetric, causing bending deformation to be accompanied by twisting. Symmetric laminates can minimize this coupling most effectively, but they often require more complex stacking arrangements, such as [0/45/−45/90]s. In this study, the [0/90] and [45/−45] layups were selected as balanced laminate configurations to reduce the influence of bending-twisting coupling while maintaining a simple and interpretable experimental design. These configurations allowed the study to focus mainly on the comparison between bending-dominated and shear-dominated impact responses. Therefore, although minor coupling effects may still occur because of hybrid material arrangement and local damage evolution, the selected balanced layups helped limit their influence on the overall bending-impact behavior.

2.2 *Fabrication of the double hat hybrid composite and material properties*

The hybrid composite specimens were fabricated using a vacuum infusion process, as shown in Figure 3. The fabrication setup consisted of a vacuum pump with a capacity of 108 L/min, a 1 L resin trap, and a resin container. Carbon fiber and glass fiber fabrics were prepared according to the designed layup sequences before infusion. The resin inlet tube was connected to the resin container, while the outlet tube was connected to the resin trap. The resin mixture was prepared by combining the base resin and catalyst at a weight ratio of 200:70 and stirring the mixture in one direction for three minutes.

After mixing, the resin was transferred to the resin container, and the vacuum pump was activated to remove air from the sealed laminate and draw the resin into the composite. The laminate was wrapped with resin absorption cloth, flow mesh, and release film to support resin flow and fiber wetting. A constant vacuum pressure of −0.2 bar was maintained throughout the infusion process. After the resin had fully saturated the laminate, the inlet and outlet tubes were disconnected, and the specimen was left to cure for 48 h. The vacuum bag, flow mesh, resin absorption cloth, and release film were then removed, and the mold was separated from the composite part. The completed double hat structures were trimmed and prepared for mechanical testing.

To improve reproducibility, key material and processing parameters are provided. The

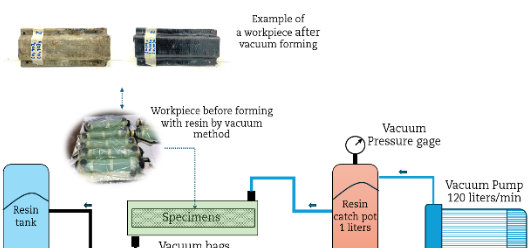

Figure 3: Vacuum infusion process used for fabricating the hybrid composite structure.

unidirectional carbon fiber and glass fiber fabrics were commercially available materials sourced from a local supplier.

The carbon fiber fabric had an areal weight of 300 g/m², elongation of 1.95%, fiber thickness of 0.167 mm, nominal ply thickness of approximately 0.25 mm, and density of 1.89 g/cm³. The glass fiber fabric had an areal weight of 350 g/m², elongation of 2.60%, fiber thickness of 0.20 mm, nominal ply thickness of approximately 0.30 mm, and density of 2.60 g/cm³.

The resin system consisted of a low-viscosity epoxy resin and compatible hardener at a weight ratio of 200:70. Its viscosity was approximately 700 mPa·s at room temperature, which is suitable for vacuum-assisted resin infusion because it supports fiber wetting and reduces void formation. The fiber volume fraction of the laminates was approximately 55%. After curing at room temperature for 48 h, post-curing was conducted at 80 °C for 2 h to enhance mechanical properties and ensure complete resin cross-linking.

Manufacturing defects such as voids, poor fiber wetting, resin-rich regions, and interlaminar delamination can reduce load transfer between laminate layers, decrease energy absorption capacity, and accelerate damage propagation during impact loading. To minimize these effects, the vacuum infusion process was used to reduce air entrapment and improve resin distribution. The resin ratio, vacuum pressure, infusion procedure, curing time, and post-curing condition were controlled consistently for all specimens. Although void content was not directly measured, the controlled fabrication process helped improve laminate uniformity and reduce the possible influence of manufacturing defects on the comparative impact results.

The mold was made of steel to provide sufficient rigidity and dimensional stability during fabrication. After curing, the laminates were trimmed to the required dimensions using a diamond cutting saw to ensure precise geometry and minimize edge defects. The final laminate thickness varied according to the stacking sequence and number of layers, with average values of approximately 0.6 mm for 2-layer configurations, 1.2 mm for 4-layer configurations, and 1.8 mm for 6-layer configurations. Minor thickness variations were observed due to manual layup and vacuum infusion. To ensure consistency in the finite element model, the material properties used in the simulations were adopted from published literature rather than experimentally measured in this study.

2.3 *Font and line spacing impact testing machine*

The impact tests were performed using a drop-type testing system, in which a weighted hammer was released from a specified height to strike the specimen. The generated impact load was recorded and used to calculate the total energy absorption and specific energy absorption of the composite structures. As shown in Figure 4, the apparatus consisted of a vertical tower with a height of 3.5 m, a pulley system for lifting the hammer, and a lower support base. A load cell with a maximum capacity of 5000 kg was installed beneath the specimen to record the impact force.

The specimen was placed freely on the support base without mechanical clamping to replicate realistic bending-impact conditions and avoid artificial constraint-induced stiffness. Under this free-support condition, load transfer occurred naturally through contact between the specimen and the support, allowing bending-dominated deformation similar to that observed in automotive side-impact scenarios. In contrast, mechanical clamping could increase local stiffness, alter the load path, and suppress bending-induced deformation, leading to non-representative failure modes.

To evaluate repeatability, three specimens with identical geometry and laminate configuration were initially tested under the same impact conditions. The resulting load–time responses were compared. If the deviation between individual curves exceeded 5%, additional specimens were tested until the response trends converged within the 5% threshold. The experimental results reported in this study therefore represent average responses from repeated tests.

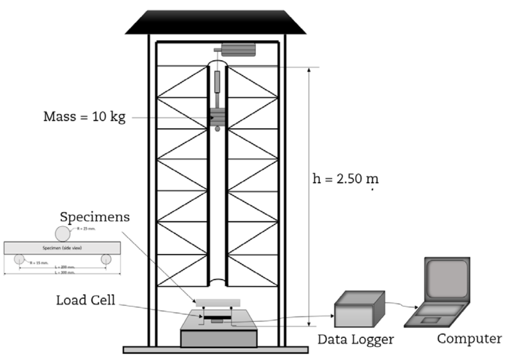

Figure 4: Drop-weight impact testing apparatus used to evaluate the composite specimens.

The force signals measured by the load cell were transmitted to a GREENTECH GTDL 350 data logger to record the dynamic load–time response.

Due to limitations of the equipment in recording time-resolved displacement during the short impact duration, the crushing distance was measured directly after the test using standard measuring instruments. The permanent deformation distance of the collapsed specimen was used as the crushing distance in the energy absorption calculation. To ensure reliability, the measured crushing distance was compared with the deformation predicted by the finite element analysis (FEA) model before being used in Equation (1). Total energy absorption and specific energy absorption were then calculated using Equations (1) and (2) [55]–[57].

The impact energy was determined from a hammer mass of 10 kg and an impact velocity of 5.42 m/s, corresponding to 147 J. The selected impact velocity represents a low-velocity impact condition commonly used in laboratory-scale testing of composite automotive structures. Previous studies on composite impact behavior commonly apply impact velocities within the range of approximately 1–10 m/s to activate damage mechanisms such as matrix cracking, fiber fracture, delamination, and progressive crushing without causing complete penetration or uncontrolled catastrophic failure. Therefore, the selected velocity was considered suitable for evaluating the bending-impact response of the double hat structure under conditions relevant to automotive side-impact components at the laboratory scale. This condition was selected to ensure complete structural collapse without catastrophic fragmentation. Preliminary tests at the maximum tower height of 3 m, corresponding to an impact velocity of approximately 7.67 m/s, caused excessive damage and severe fragmentation, making the crushing distance difficult to measure. Therefore, the impact velocity was reduced to 5.42 m/s to obtain progressive crushing deformation and reliable energy absorption data. Any previously reported impact velocity of 6.26 m/s was corrected to ensure consistency with the actual experimental condition. A high-speed camera operating at 1250 frames per second was also used to record the deformation process during impact.

$$E_a = P_{mean} \cdot S = \int P ds \quad (1)$$

$$E_s = \frac{P_{mean} \square s}{mass} \quad (2)$$

3 Finite Element Analysis

3.1 *Material properties*

The material properties of the double hat composite structure were defined in the finite element model based on the unidirectional carbon and glass fiber laminates used in this study. Since the specimens were fabricated by stacking unidirectional layers, the constitutive model and damage parameters were defined using a failure theory suitable for fiber-reinforced composites. In this study, the mechanical properties and damage criteria for both carbon and glass fiber laminates were implemented using the Hashin failure theory.

The Hashin failure criterion was selected because it is widely used for predicting progressive damage initiation in fiber-reinforced composite laminates under dynamic impact loading. The model evaluates four failure mechanisms: fiber tension, fiber compression, matrix tension, and matrix compression. These mechanisms are suitable for capturing the damage behavior of hybrid CFRP/GFRP laminates subjected to bending impact. The governing equations for the Hashin damage criteria are presented in Equations (3)-(6).

Fiber tension damage $(\hat{\sigma}_{11}) \geq 0$:

$$F_f^t = (\frac{\hat{\partial}_{11}}{X^T})^2 + (\alpha \frac{\hat{\tau}_{12}}{S^L})^2 \quad (3)$$

Fiber tension compression $(\hat{\sigma}_{11}) \leq 0$:

$$F_f^c = (\frac{\hat{\sigma}_{11}}{x^c})^2 \quad (4)$$

Matrix tension $(\hat{\sigma}_{22}) \geq 0$:

$$F_m^t = (\frac{\hat{\sigma}_{22}}{Y^T})^2 + (\alpha \frac{\hat{\tau}_{12}}{S^L})^2 \quad (5)$$

Matrix tension $(\hat{\sigma}_{22}) \leq 0$:

$$F_m^c = (\frac{\hat{\sigma}_{22}}{2S^T})^2 + [(\frac{Y^C}{2S^L})^2 - 1]\frac{\hat{\sigma}_{22}}{Y^C} + (\frac{\hat{\tau}_{12}}{S^L})^2 \quad (6)$$

In the Hashin failure model, the failure indices represent the onset of fiber tension, fiber compression, matrix tension, and matrix compression damage. The parameters X_T, X_C, Y_T, Y_C, S_L, and S_T refer to the longitudinal tensile strength, longitudinal compressive strength, transverse tensile strength, transverse compressive strength, longitudinal shear strength, and transverse shear strength, respectively. The parameter αdefines the contribution of shear stress to fiber tensile damage initiation. The symbols σ_{11}, σ_{22}, and τ_{12} represent the effective stress components in the fiber direction, transverse direction, and in-plane shear direction.

For the damage initiation behavior of fiber-reinforced polymer composites, carbon fiber and glass fiber were evaluated using the corresponding damage equations. Since the laminate response mainly follows plane stress conditions, damage initiation was assessed using the plane-stress form of the Hashin criteria, as expressed in Equations (5) and (6). The constitutive stiffness degradation relationship used in the model is given in Equation (7).

$$C_d = \frac{1}{D}\begin{pmatrix} (1-d_f)E_{11} & (1-d_f)(1-d_m)\upsilon_{21}E_{11} & 0 \\ (1-d_f)(1-d_m)\upsilon_{12}E_{12} & (1-d_m)E_{12} & 0 \\ 0 & 0 & (1-d_s)E_3 \end{pmatrix} \quad (7)$$

In the constitutive model, the term $(1 - d_f)(1 - d_m)E_{11}$ represents the reduced stiffness caused by accumulated fiber and matrix damage. The parameter $d_f$reflects the current state of fiber damage, $d_m$reflects matrix damage, and d_s reflects shear damage. The symbols $E_{11}$and E_{22} refer to Young's modulus in the longitudinal and transverse directions, respectively. The parameters $G_{12}$and G_{23} denote the in-plane and out-of-plane shear moduli, while the remaining terms represent the Poisson's ratios of the composite material.

The values of d_f, d_m, and $d_s$were calculated based on the damage variables d_{ft}, d_{fc}, d_{mt}, and d_{mc}. These variables correspond to fiber tension damage, fiber compression damage, matrix tension damage, and matrix compression damage, respectively. The relationships used to evaluate these damage variables are given in Equations (8)-(10).

$$d_f = \begin{cases} d_f^t \; if \; \hat{\sigma}_{11} \geq 0 \\ d_f^c \; if \; \hat{\sigma}_{11} < 0 \end{cases} \quad (8)$$

$$d_m = \begin{cases} d_m^t \; if \; \hat{\sigma}_{22} \geq 0 \\ d_m^c \; if \; \hat{\sigma}_{22} < 0 \end{cases} \quad (9)$$

$$d_s = 1 - (1 - d_f^t)(1 - d_m^t)(1 - d_m^c) \quad (10)$$

The damage variable represents the degree of material degradation and can be determined from the corresponding damage evolution equation, as shown in Equation (11).

$$d = \frac{\delta_{eq}^f(\delta_{eq} - \delta_{eq}^0)}{\delta_{eq}(\delta_{eq}^f - \delta_{eq}^0)} \quad (11)$$

In Equation (11), the term δ^0refers to the initial equivalent displacement at which the damage initiation criterion is reached, while δ^f represents the equivalent displacement at complete material degradation. The relationship between these displacement variables and the damage evolution process is illustrated in Figure 5. Damage evolution was governed by a linear stiffness degradation law after Hashin damage initiation, allowing progressive stiffness reduction to be captured during impact loading. This formulation is consistent with commonly used approaches in composite impact simulations.

Based on this damage modeling framework, material properties were defined for carbon fiber reinforced polymer and glass fiber reinforced polymer laminates. The material input properties used in the finite element model were adopted from well-established experimental studies on CFRP and GFRP laminates. The damage evolution parameters used in the simulations are summarized in Tables 2 for carbon fiber and glass fiber, respectively. Both composite systems used unidirectional fabrics, consistent with the material properties reported by Sakkampang and Onsalung [58]. The use of unidirectional fabrics also allowed straightforward definition of material orientation in the numerical model. It should be noted that all material properties listed in Tables 3 were adopted from published literature and were not experim entally measured in the present study. These parameters were selected because they are suitable for representing the mechanical behavior of CFRP and GFRP laminates under impact loading conditions. Table 2 presents the density and elastic properties of CFRP and GFRP, while the corresponding strength and damage parameters are provided in the following tables. Based on the listed properties, carbon fiber has a higher modulus than glass fiber, while both materials have comparable densities, making them suitable for hybridization without introducing significant weight differences.

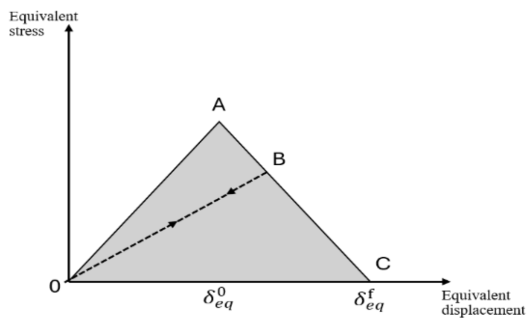

Figure 5: Linear damage evolution law showing equivalent stress versus equivalent displacement.

Table 2: Material properties of carbon fiber reinforced (CFRP) and glass fiber reinforced (GFRP).

Property	Description	CFRP	GFRP
ρ	Density (kg/m^3)	1,800	1,800
E_{11}	Young's modulus in longitudinal (fiber) direction (GPa)	66.34	66.34
E_{12}	Young's modulus in transverse direction (GPa)	7.153	7.153
G_{12}	In-Plane shear modulus (GPa)	9.653	9.653
G_{23}	Out of Plane shear modulus (GPa)	2.458	2.458
ν_{12}	Poisson's ratio	0.27	0.27
X^T	Longitudinal tensile strength (MPa)	1142.14	721.55
X^C	Longitudinal compressive strength (MPa)	263.78	138.11
Y^T	Transverse tensile strength (MPa)	18.23	13.78
Y^c	Transverse compressive strength (MPa)	35.25	13.81
S^L	Longitudinal Shear strength (MPa)	28.83	12.01
S^T	Transverse Shear strength (MPa)	30.50	24.02

3.2 *Finite element model development*

The finite element model was developed by replicating the specimen geometry and experimental variables used in the impact tests. Numerical simulations were conducted using ABAQUS/Explicit, which is suitable for high-speed impact problems involving large deformation and complex contact behavior. As shown in Figure 6, the model consisted of three main components: the double hat structure, the support, and the impact hammer. The double hat structure was modeled using the same dimensions as the fabricated specimens and included the hybrid layups of carbon fiber and glass fiber with different stacking sequences and fiber orientations. The support was modeled as a cylindrical structure representing the load cell base, while the hammer was modeled as a cylindrical body used to apply the impact load. Shell elements with reduced integration were used for the composite laminates because of the thin-walled geometry of the double hat structure. This element formulation is suitable for capturing bending, c rushing, and large deformation behavior with reasonable computational cost.

The fiber orientations considered in this study were 0°, 90°, 45°, and −45°. In the finite element model, each laminate layer was assigned a local coordinate system. The X-axis was aligned with the longitudinal direction of the specimen, while the Y-

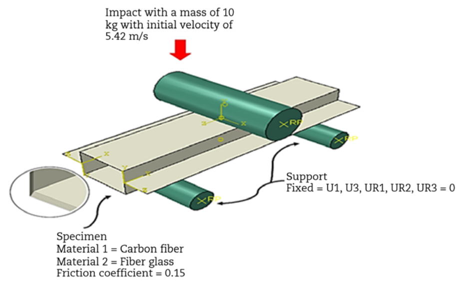

Figure 6: Finite element model illustrating the applied impact loading, boundary conditions,material assignment, and contact definitions used in the simulation.

Table 3: Energy absorption capacity of the double hat structures under bending impact.

Specimens	**Experimental**				**FEA**				**R-square**
	Average Load (kN)	**Peak Load (kN)**	**Energy Absorption (kJ)**	**Specific Energy Absorption (kJ/kg)**	**Average Load (kN)**	**Peak Load (kN)**	**Energy Absorption (kJ)**	**Specific Energy Absorption (kJ/kg)**	
2- layer									
CC[45/-45]$_2$	-	-	-	-	0.466	1.349	0.022	0.074	-
GG[45/-45]$_2$	-	-	-	-	0.513	1.673	0.016	0.056	-
CG[45/-45]$_2$	-	-	-	-	0.476	1.446	0.019	0.065	-
GC[45/-45]$_2$	-	-	-	-	0.581	1.511	0.018	0.063	-
4- layer									
CC[0/90]$_4$	0.636	2.846	0.061	0.174	0.891	2.911	0.066	0.188	0.953
GG[0/90]$_4$	0.911	3.482	0.054	0.154	1.141	3.432	0.055	0.159	0.826
CG[0/90]$_4$	0.952	3.025	0.059	0.169	1.090	3.145	0.062	0.179	0.920
GC[0/90]$_4$	0.983	3.100	0.056	0.161	1.192	3.003	0.058	0.167	0.804
CC[45/-45]$_4$	1.147	3.140	0.145	0.364	1.451	3.365	0.146	0.366	0.826
GG[45/-45]$_4$	1.329	4.220	0.074	0.214	1.539	4.501	0.095	0.191	0.811
CG[45/-45]$_4$	1.724	4.027	0.091	0.261	1.528	3.407	0.107	0.268	0.923
GC[45/-45]$_4$	1.327	3.390	0.086	0.247	1.736	4.118	0.100	0.250	0.842
6- layer									
CCC[0/90]$_6$	0.738	2.293	0.058	0.130	0.945	2.221	0.060	0.135	0.814
GGG[0/90]$_6$	0.843	2.930	0.038	0.077	1.145	2.957	0.044	0.089	0.895
CGC[0/90]$_6$	0.559	2.352	0.044	0.099	0.703	2.466	0.049	0.109	0.920
GCG[0/90]$_6$	0.586	2.637	0.040	0.090	0.789	2.535	0.046	0.102	0.865
CCC[45/-45]$_6$	1.114	2.837	0.089	0.223	1.132	2.723	0.095	0.237	0.758
GGG[45/-45]$_6$	1.145	3.846	0.076	0.152	1.592	3.915	0.078	0.156	0.870
CGC[45/-45]$_6$	1.149	2.927	0.080	0.201	1.412	2.940	0.082	0.205	0.784
GCG[45/-45]$_6$	1.372	3.084	0.079	0.199	1.435	3.607	0.079	0.198	0.876

Applied Science and Engineering Progress, Vol. 20, No. 3, 2027, 8277

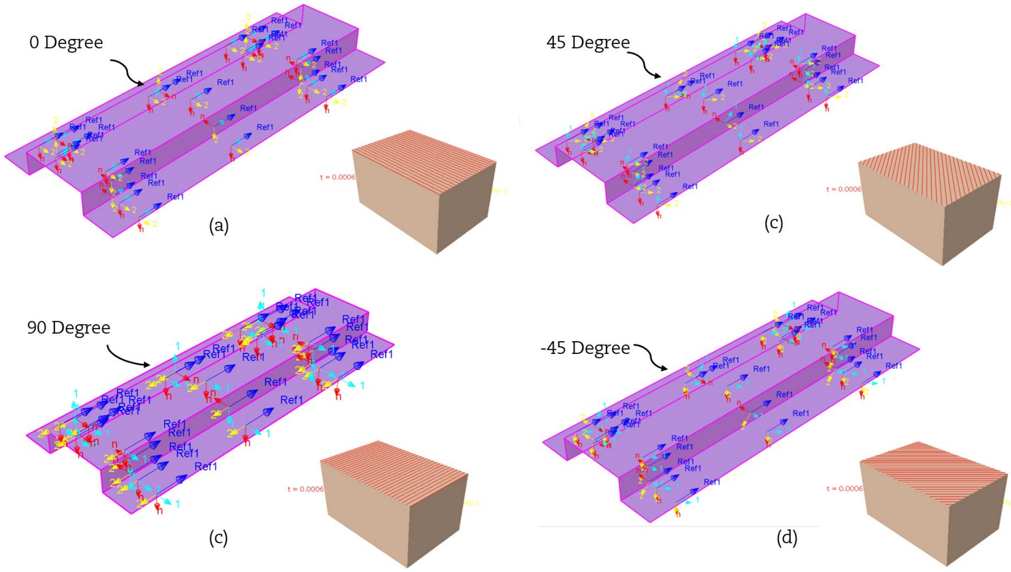

Figure 7: Fiber orientation directions defined in the finite element model: (a) 0 degrees, (b) 45 degrees, (c) 90 degrees, and (d) -45 degrees.

axis represented the transverse direction. Directions 1, 2, and 3 corresponded to the longitudinal, transverse, and thickness directions, respectively. As shown in Figure 7, the reference axis represented the longitudinal direction of the double hat structure, and Axis 1 corresponded to the assigned fiber orientation of each layer.

Figure 6 presents the main parameters defined in the finite element model. The analysis was performed using an explicit dynamic formulation to capture large deformation and nonlinear contact interactions during impact. The hammer was assigned a mass of 10 kg and an impact velocity of 5.42 m/s, corresponding to an impact energy of approximately 147 J. This energy level was selected to ensure complete structural collapse without catastrophic fragmentation and to allow comparison between experimental and numerical results. The hammer was constrained to move only along the Y-axis to reproduce the vertical motion of the experimental drop tower system.

The support was fully constrained in all translational and rotational degrees of freedom. The specimen was placed on the support without translational or rotational constraints or mechanical clamping, replicating the free-support experimental condition. This setup avoided artificial constraint-induced stiffness and allowed natural load transfer through contact interaction, progressive folding, and bending-dominated deformation under impact loading. Surface-to-surface contact interactions were defined between the hammer, specimen, and support. A friction coefficient of 0.2 was adopted based on reported metal–composite contact values in the literature. No mass scaling was used in the explicit dynamic simulations to avoid artificially altering the inertial effects and dynamic response.

The contact definitions and boundary conditions were established to closely reproduce the experimental setup. The free-support condition used in this study differs from conventional fully clamped boundary conditions and allows more realistic deformation and load redistribution during bending impact. Quantitative validation of the finite element model was performed by comparing load–time

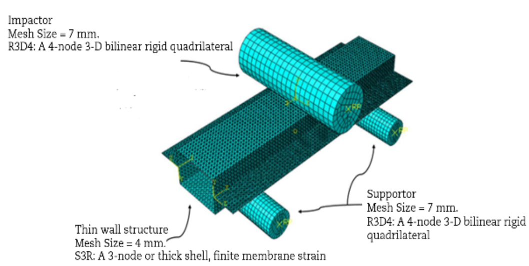

Figure 8: Mesh configuration of the finite element model showing the composite structure and support components used in the impact simulation.

responses, absorbed energy, deformation patterns, and collapse modes between the simulations and experimental observations.

Mesh generation was important because mesh size directly affects the accuracy of deformation and damage prediction. As shown in Figure 8, mesh refinement was applied to the composite structure, where significant deformation and failure occurred. A mesh sensitivity study was conducted by varying the element size from 10 mm to 3 mm. The load–time responses, absorbed energy, and deformation patterns were compared with the experimental results. Reducing the mesh size from 10 mm to 4 mm improved the correlation between numerical and experimental results, while further refinement below 4 mm produced no noticeable change in peak load, absorbed energy, or collapse mode. Therefore, a mesh size of 4 mm was selected as the optimal balance between numerical accuracy and computational efficiency and was used for all simulations. The convergence criterion was defined as the point at which further mesh refinement produced only negligible changes in the main response indicators. In this study, the differences in peak load, absorbed energy, and final deformation pattern between the 4 mm and 3 mm meshes were small and did not affect the interpretation of the results. Therefore, the 4 mm mesh was considered sufficiently converged for the composite specimen. This criterion was selected because the objective of the model was to reproduce the global impact response and failure pattern rather than to predict highly localized microscopic damage.

Model validation was performed by comparing deformation shapes, collapse modes, and absorbed energy between the numerical simulations and experimental observations. The correlation between numerical predictions and experimental results exceeded 95%, confirming the suitability of the selected mesh size and modeling approach. A mesh size of 7 mm was assigned to the hammer and support because these components were modeled as rigid bodies and did not undergo deformation. Further refinement of these parts was therefore unnecessary. The specimen–support interface was modeled without constraints to replicate the free-support experimental condition.

4 Results and discussion

4.1 *Load response: average load and peak load*

4.1.1 Load response of 4-layer laminates

The impact response of the 4-layer hybrid laminates was examined for two stacking patterns: [0/90] and [45/−45]. Figure 9 compares the experimental results and finite element predictions in terms of load–time curves, deformation patterns, and damage development. All experimental values represent mean responses obtained from repeated tests, with deviations within 5%. The numerical results are summarized in Table 3.

For the [0/90] orientation shown in Figure 9 (a), the initial segment of the load–time curve corresponded to the undamaged elastic region, where no visible damage occurred and the material response remained linear. After this stage, the load decreased as the structure progressively collapsed under impact. Based on the peak load values, the glass fiber laminate showed the highest load among the carbon fiber, glass fiber, and hybrid configurations. The GG$[0/90]_4$ specimen achieved a peak load of 3.482 kN and an average load of 0.911 kN. The carbon fiber laminate CC$[0/90]_4$ produced a peak load of 2.846 kN and an

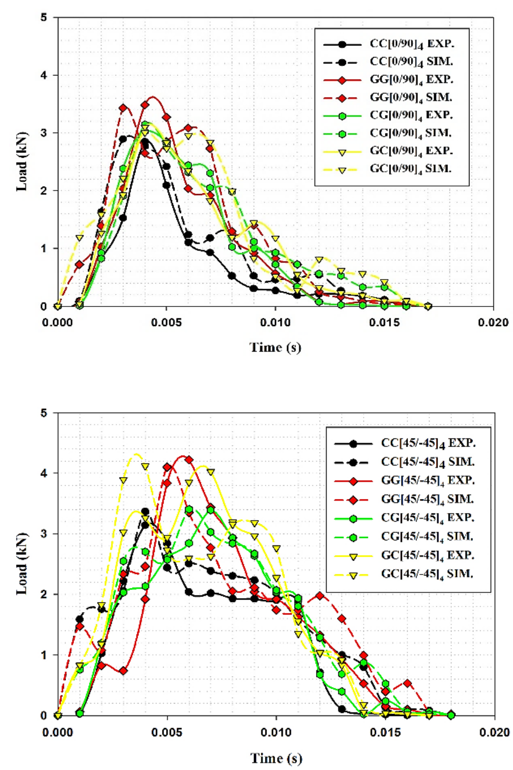

Figure 9: Load–time responses of the 6-layer hybrid laminate configurations. (a) 6-layer hybrid laminate with the [0/90] orientation. (b) 6-layer hybrid laminate with the [45/-45] orientation.

average load of 0.636 kN. For the hybrid laminates, CG[0/90]$_4$ and GC[0/90]$_4$ showed peak and average loads lower than those of the full glass fiber laminate but slightly higher than those of the full carbon fiber laminate. Both the experimental results and the finite element model showed consistent response patterns across all 4-layer [0/90] configurations.

Figure 9(b) presents the responses of the [45/−45] laminates. Comparison between the experimental and numerical results showed two characteristic behaviors at the initial stage of the load–time curve. In some cases, the load increased steadily until the laminate reached its ultimate strength before damage initiation. In other cases, the curve slope changed rapidly because the hammer retained residual inertia, causing a temporary rise in the recorded load before structural collapse. The initial shift observed in the CG[45/−45]$_4$ and GC[45/−45]$_4$ curves was mainly related to differences in initial contact stiffness and stress wave propagation caused by the stacking sequence and material arrangement. Since carbon fiber and glass fiber have different elastic moduli and deformation characteristics, the outer contact layer influenced early-stage load transfer during impact. After this stage, the curves entered the failure region, where fracture, folding, and crushing reduced the load.

For the hybrid laminates, CG[45/−45]$_4$ exhibited a peak load of 4.027 kN and an average load of 1.724 kN, while GC[45/−45]$_4$ produced a peak load of 3.390 kN and an average load of 1.327 kN. The shear-dominated response of the [45/−45] configuration was consistent with previous studies on hybrid composite hat structures. These results indicate that the [45/−45] orientation produced higher load responses in the 4-layer laminates because the angled fibers promoted shear load transfer during impact. In contrast, the [0/90] configuration showed more bending-dominated behavior through horizontal and vertical fiber directions.

It should be noted that the impact tests in this study were fully dynamic, and energy absorption was calculated from the measured impact force using Equation (1). Due to limitations of the experimental setup, time-resolved displacement data could not be recorded during the short impact duration. Therefore, direct construction of energy–time curves was not feasible. Energy–time relationships are more commonly obtained in quasi-static compression tests, where displacement can be measured incrementally using devices such as LVDTs. Accordingly, this study evaluated energy absorption using total absorbed energy and specific energy absorption, which are appropriate metrics for dynamic impact experiments.

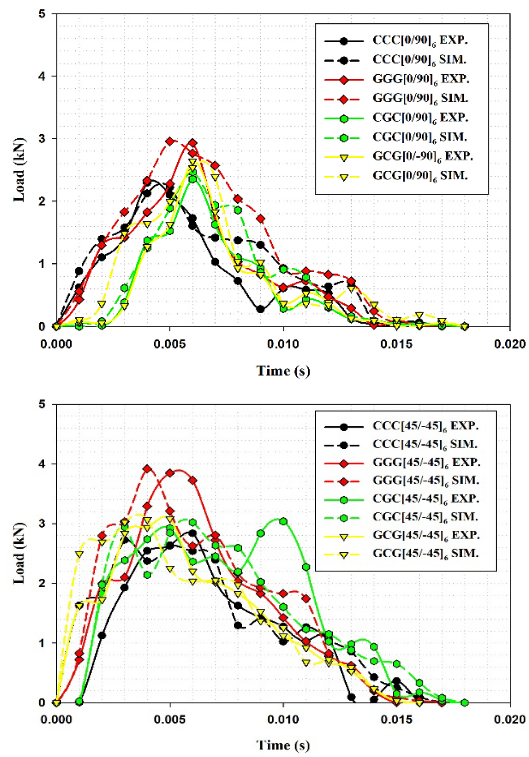

Figure 10: Load–time responses of the 6-layer hybrid laminate configurations. (a) 6-layer hybrid laminate with the [0/90] orientation. (b) 6-layer hybrid laminate with the [45/-45] orientation.

4.1.2 Load response of 6-layer laminates

Figure 10 presents the load–time responses obtained from the experimental tests and finite element simulations under bending impact. All experimental values represent average responses from repeated tests, with deviations remaining within an acceptable range for dynamic impact experiments.

For the [0/90] orientation shown in Figure 10(a), the GGG[0/90]$_6$ configuration produced the highest load values among the 6-layer laminates, with a peak load of 2.930 kN and an average load of 0.843 kN. These values were higher than those of the CCC[0/90]$_6$ laminate, which produced a peak

Applied Science and Engineering Progress, Vol. 20, No. 3, 2027, 8277

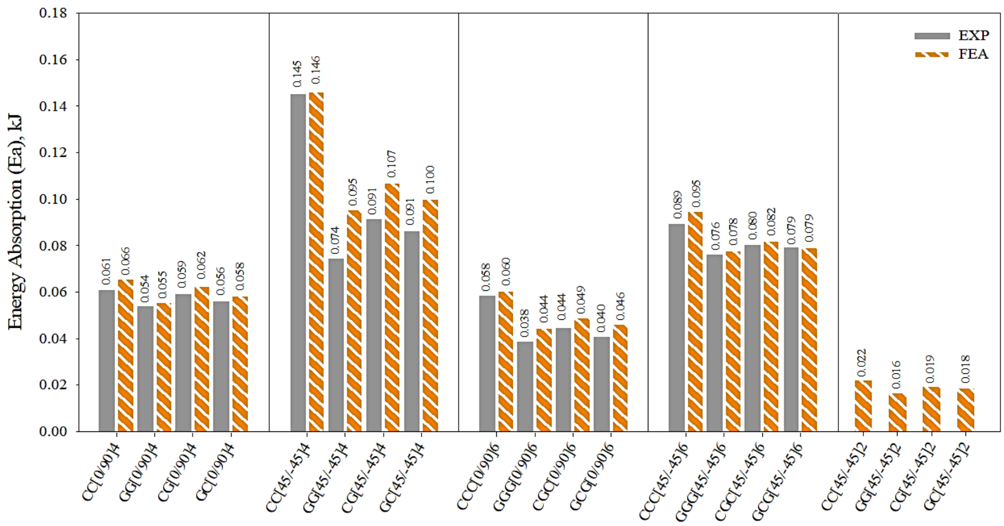

Figure 11: Energy absorption of the double hat structures with two-layer, four-layer, and six-layer fiber orientations.

load of 2.293 kN and an average load of 0.738 kN. Among the 6-layer [0/90] configurations, the carbon fiber laminate CCC$[0/90]_6$ showed the lowest peak load.

Figure 10(b) shows the responses of the [45/−45] configurations. For this orientation, the GGG$[45/-45]_6$ laminate provided the highest impact resistance, with a peak load of 3.846 kN and an average load of 1.45 kN. Compared with the [0/90] laminates, the [45/−45] configurations generally produced higher peak loads, indicating that the angled fiber directions had a stronger influence on the impact response of the 6-layer laminates. The [0/90] and [45/−45] configurations represent bending-dominated and shear-dominated load-transfer mechanisms, respectively.

The finite element results showed good agreement with the experimental data for both fiber orientations. Minor deviations may be attributed to differences in mesh size, friction parameters, or contact behavior in the model. Model validation was not limited to the load–time curves but also included qualitative and quantitative comparisons of deformation shape, collapse mode, and absorbed energy. The finite element model successfully reproduced the progressive folding behavior, bending deformation, and final collapse configurations observed in the experiments. The absorbed energy predicted by the simulations also showed close agreement with the measured values, confirming the reliability of the numerical model in capturing the global impact response. In this study, mesh size and friction parameters were calibrated to provide the closest agreement with the experimental load–time curves, resulting in reliable finite element predictions consistent with the test results shown in Figure 10.

4.2 *Energy absorption (E_a)*

Energy absorption refers to the amount of energy a Energy absorption refers to the amount of energy absorbed by a structure during impact or crushing. In this study, the energy absorption of the hybrid double hat structures was determined from the area under the load–displacement curve and calculated by multiplying the average load (P_{mean}) by the crushing distance (S). Table 3 presents the energy absorption values obtained from both the experimental tests and finite element simulations for the 4-layer and 6-layer configurations.

To extend the investigation beyond the experimental conditions, a finite element model was also developed for a two-layer configuration. This analysis was conducted to determine whether reducing the number of layers could lower material cost while maintaining acceptable impact resistance. Hybrid CFRP/GFRP laminates can reduce overall material cost by partially replacing carbon fiber with lower-cost glass fiber while maintaining comparable energy absorption performance.

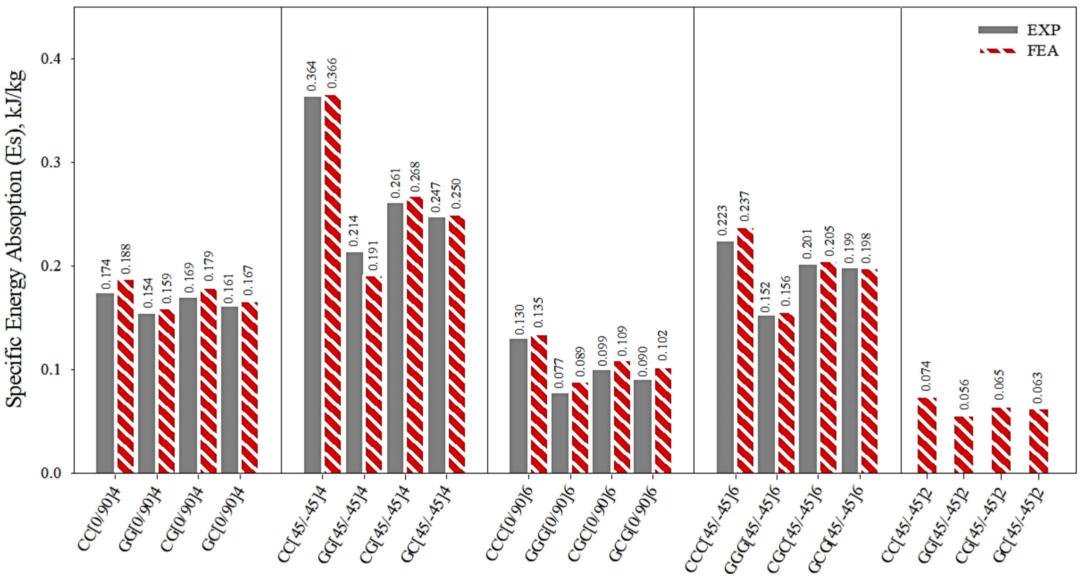

Figure 12: Specific energy absorption of the double hat structures with two-layer, four-layer, and six-layer fiber orientations.

Figure 11 shows that the [45/−45] orientation produced the highest energy absorption among the stacking patterns. Based on the experimental data, the carbon fiber laminate CC[45/−45]$_4$ provided the greatest energy absorption, with a value of 0.145 kJ. For the hybrid laminates, CG[45/−45]$_4$ and GC[45/−45]$_4$ absorbed 0.091 kJ and 0.086 kJ, respectively, while the glass fiber laminate GG[45/−45]$_4$ showed the lowest value, at 0.074 kJ. These values are consistent with the results reported in Table 3.

The results confirm that fiber orientation directly affects energy absorption capability. The [45/−45] configuration absorbed energy more effectively than the [0/90] configuration because its angled fibers promoted shear-dominated deformation, progressive folding, and more stable crushing. This finding is consistent with previous studies on hybrid composite hat structures. C. Qi et al. [34] reported that shear-dominated fiber orientations in composite double-hat structures enhance progressive folding and energy absorption compared with bending-dominated configurations.

The superior performance of the [45/−45] configuration can be attributed to its ability to redistribute impact-induced stresses through diagonal shear paths. During bending impact, the angled fiber arrangement promotes progressive shear deformation and delays catastrophic longitudinal cracking, allowing the structure to sustain deformation over a longer crushing distance. In contrast, the [0/90] configuration tends to concentrate stresses along the principal fiber directions, leading to earlier longitudinal and transverse cracking, localized failure, and reduced crushing displacement.

4.3 *Specific energy absorption (E_s)*

Specific energy absorption represents the amount of energy absorbed by a structure relative to its mass. It is calculated as the ratio of total energy absorption (Ea) to the specimen mass (m). This parameter is important for selecting lightweight structural configurations because it reflects the energy absorption efficiency per unit mass. Figure 12 presents the specific energy absorption obtained from the experimental tests and finite element simulations under bending impact for the [45/−45] orientation. All experimental values represent average responses from repeated tests.

The experimental results showed that the CC[45/−45]$_4$ configuration provided the highest specific energy absorption, with a value of 0.364 kJ/kg. For the hybrid laminates, CG[45/−45]$_4$ and GC[45/−45]$_4$ showed values of 0.261 and 0.247 kJ/kg, respectively. The glass fiber laminate

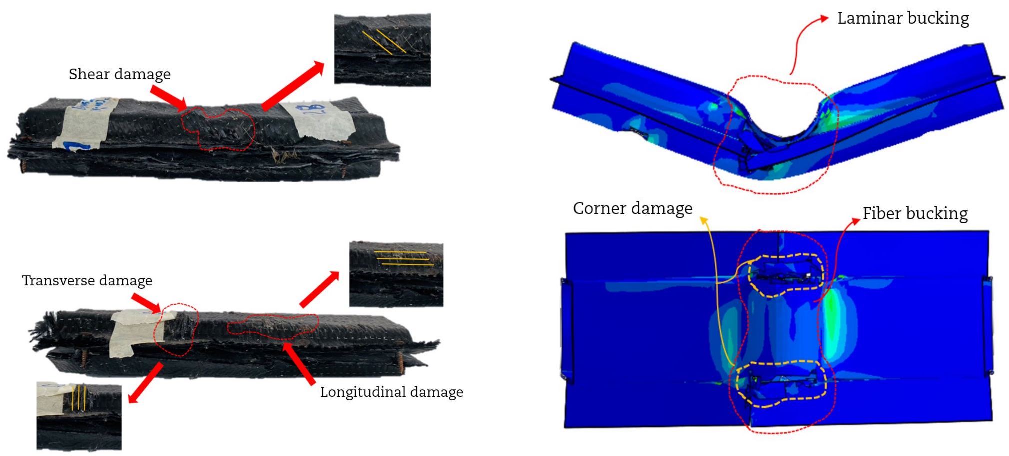

Figure 13: Failure behavior of the 4-layer double hat structures with the [0/90] fiber orientation.

GG[45/−45]$_4$ produced the lowest value among the 4-layer [45/−45] laminates, at 0.214 kJ/kg. These results confirm that the [45/−45] orientation provides better specific energy absorption than the [0/90] orientation because of its shear-dominated load-transfer mechanism.

For the 6-layer laminates, a similar trend was observed. The CCC[0/90]$_6$ specimen recorded a specific energy absorption of 0.135 kJ/kg. The hybrid configurations CGC[0/90]$_6$ and GCG[0/90]$_6$ showed values of 0.105 and 0.102 kJ/kg, respectively, while the glass fiber laminate GGG[0/90]$_6$ provided the lowest value, at 0.089 kJ/kg. The finite element simulation results were consistent with the experimental findings.

The finite element model was also used to examine the behavior of two-layer laminates. Compared with the 4-layer and 6-layer specimens, the two-layer configuration showed much lower specific energy absorption. This result agrees with the total energy absorption results, indicating that reducing laminate thickness below four layers leads to insufficient structural capacity and excessive load transfer during impact. In contrast, increasing laminate thickness increases stiffness and reduces crushing displacement, which can limit the total absorbed energy.

Specific energy absorption is an important indicator because it reflects the ability of a material or structure to absorb energy per unit mass. For structures with the same mass, the laminate that absorbs the greatest amount of energy is considered the most efficient. Based on Figure 12 and Table 3, the [45/−45] orientation provided the best performance in terms of energy absorbed per unit mass. The analysis also confirms that 4-layer laminates offer the most suitable balance between structural capacity, energy absorption, and material usage. The energy absorption values reported in Section 4.2 were verified against Table 3 to ensure consistency.

4.4 *Failure behavior*

The failure behavior of the double hat composite structures was examined using both laboratory tests and finite element simulations. This section discusses the representative failure modes observed in the 4-layer and 6-layer configurations with [0/90] and [45/−45] fiber orientations. The GC[0/90]$_4$ specimen was selected as a representative 4-layer case because it showed clear and complete failure patterns.

Failure behavior of the 4-layer double hat structures with the [0/90] and [45/−45] fiber orientations was presented in Figure 13. For the 4-layer [0/90] configuration, two main damage types were identified after full collapse. The first was longitudinal damage, which propagated along the length of the specimen or along the 0° fiber direction [59], [60]. This damage mainly occurred at the corners and at the junction between the upper and

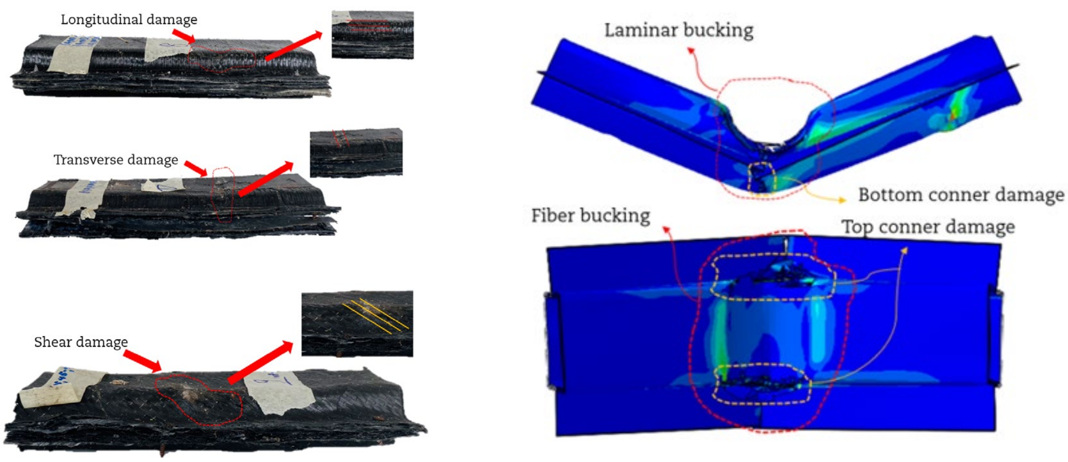

Figure 14: Failure behavior of the 6-layer double hat structures with the [0/90] and [45/−45] fiber orientations.

lower hat sections, where stress concentration was high. The second was transverse damage, which developed across the specimen at 90° [61] and was mainly observed on the surface directly impacted by the hammer.

The finite element simulations captured these damage behaviors at different stages of deformation. When the carbon fiber layer was placed on the outer contact surface, high stress concentration appeared at the corners and at the connection between the two hat sections during crushing. In contrast, when glass fiber was used as the outer contact layer, as in the GC[0/90]$_4$ configuration, the simulated von Mises stress values were lower, ranging from 0.689 to 0.709 GPa. This indicates that glass fiber dissipates stress differently from carbon fiber.

Two major damage mechanisms were observed in the simulation: laminar buckling and fiber buckling. Laminar buckling occurred when the laminate bent, separated, and delaminated due to through-thickness compressive forces during collapse [62], [63]. Fiber buckling occurred when individual fibers experienced local instability, fracture, and separation under compressive loading [64], [65]. Damage evolution followed a linear stiffness degradation law after Hashin damage initiation. These simulated patterns agreed with the experimental observations, confirming that the model represented the actual failure process of the hybrid composite structures.

For the 4-layer [45/−45] configuration, the failure behavior differed from that of the [0/90] laminate. The experimental results showed damage after full collapse, followed by visible tearing at the final deformation stage. The dominant failure mode was shear damage, characterized by diagonal cracking caused by shear forces across the structure. Initial cracks formed at the center of the specimen where the hammer contacted the surface, then propagated through the shear-resistant region until the structure reached maximum collapse. This shear-dominated response is consistent with previous studies on hybrid composite hat structures.

The FEA results supported these observations. The upper hat section showed larger deformation, while the lower section showed smaller displacement. The highest stress concentrations occurred near the center of the model. When glass fiber was used as the outer surface, the simulated von Mises stress values were generally lower, although higher stress appeared near the bottom region. Surface cracking initiated at the impact zone and extended toward the upper corners of the side walls. As collapse progressed, failure propagated along the side walls and reached the flange area connecting the upper and lower hats, leading to final fracture.

Three major failure mechanisms were identified in the 4-layer [45/−45] configuration: laminar buckling, fiber buckling, and corner damage. Laminar buckling occurred when the laminate bent and separated under compressive forces. Fiber buckling involved local fiber instability and separation under compression. Corner damage involved failure at the upper corner regions and separation of fiber layers. These damage patterns confirmed the strong influence of the [45/−45] fiber orientation on shear-dominated failure behavior.

For the 6-layer structures, the experimental results showed damage after full collapse, followed by tearing at the final deformation stage. Compared with the 4-layer specimens, the 6-layer laminates exhibited lower displacement and higher load-bearing capacity. As shown in Figure 14, the [0/90] orientation produced longitudinal damage along the specimen length and transverse damage across the width. Increasing laminate thickness improved load resistance but shortened the crushing distance. Local surface cracking appeared at the impact zone during the early stage and then spread outward as deformation progressed.

Figure 14 shows the failure behavior of the 6-layer [45/−45] configuration. The dominant failure mode was shear damage, which is typical when diagonal shear forces govern the structural response. This shear-based failure allowed the structure to carry higher loads than the [0/90] orientation. Cracks initiated at the impact surface due to diagonal tension within the laminate and propagated through the shear-critical regions until final tearing occurred.

The superior impact performance of the [45/−45] configuration is strongly related to its progressive shear-dominated failure mechanism. Unlike the [0/90] configuration, which tends to concentrate stresses along the principal fiber directions and promote early longitudinal cracking, the angled fiber arrangement redistributes impact-induced stresses through diagonal shear paths. This stress redistribution delays catastrophic crack propagation and allows damage to spread progressively instead of localizing in one region. As a result, the structure maintains load-carrying capacity for a longer duration, producing greater crushing displacement and energy dissipation. The diagonal fiber orientation also promotes stable folding and controlled delamination between laminate layers, which further improves energy absorption under bending impact.

The FEA simulations agreed with the experimental findings for the 6-layer laminates. The upper hat section showed larger deformation, while the lower section showed only slight deformation. Stress concentrations were mainly located near the central region, upper corners, and side walls. When glass fiber was used as the outer contact layer, surface cracking appeared at the impact zone and propagated toward the flange area. Across the CCC$[45/-45]_6$, GGG$[45/-45]_6$, CGC$[45/-45]_6$, and GCG$[45/-45]_6$ configurations, similar damage characteristics were observed. The experimental and FEA results showed closely matching damage locations and deformation shapes, confirming that the numerical model reproduced the failure mechanisms of the 6-layer hybrid structures.

Although this study did not directly measure the interfacial bonding strength between carbon and glass fiber layers, its possible influence on damage propagation should be considered. Interfacial bonding between adjacent hybrid laminate layers plays an important role in stress transfer and delamination resistance. Weak interfacial bonding may promote interlaminar crack initiation and accelerate damage propagation during impact loading. In contrast, strong bonding can improve load transfer between carbon and glass fiber layers, enhance energy absorption, and delay crack growth under bending impact. In this study, the fractured specimens were sectioned and visually examined to observe whether interlaminar tearing occurred. However, detailed characterization of the carbon–glass interface was difficult because the laminate layers were tightly bonded, and some specimens did not show clear interlaminar separation. Therefore, the influence of interfacial bonding is discussed as a possible factor affecting damage propagation, and direct interfacial characterization is recommended for future work.

The failure behaviors observed in this study are consistent with previous experimental and numerical studies on thin-walled composite and hybrid structures under impact loading. Previous studies reported that [0/90] layups tend to exhibit longitudinal and transverse cracking due to bending-dominated deformation, whereas ±45° configurations promote shear-dominated failure and progressive energy dissipation [55,56]. Similar shear-driven damage patterns in composite hat and channel sections were reported by Deng et al. [62], where diagonal cracking delayed catastrophic failure. Compared with single-material CFRP or GFRP laminates, the present hybrid carbon–glass configurations showed improved damage tolerance and more stable progressive collapse under bending impact. In addition, the free-support boundary condition used in this study allowed more natural load transfer and representative collapse behavior than fully clamped conditions. These findings highlight the combined influence of hybrid material systems, fiber orientation, and boundary conditions on the impact response of energy-absorbing composite structures.

5 Conclusions

This study investigated the influence of fiber orientation and laminate thickness on the impact performance of hybrid composite double hat structures under bending impact using experimental testing and finite element analysis. Unlike many previous studies that focused on axial crushing or fully clamped boundary conditions, this study examined hybrid double hat structures under free-support bending-impact conditions, which more closely represent automotive side-impact scenarios.

The results confirmed that fiber orientation and laminate thickness strongly influenced impact resistance, energy absorption, and failure behavior. The [45/−45] orientation provided higher energy absorption and specific energy absorption than the [0/90] orientation because its shear-dominated load-transfer mechanism promoted progressive deformation and delayed structural collapse. In contrast, the [0/90] orientation mainly exhibited longitudinal and transverse cracking with lower energy absorption capability.

Laminate thickness also affected the structural response. Increasing the number of layers improved load-bearing capacity but reduced crushing displacement because of increased stiffness. Therefore, excessive laminate thickness did not necessarily improve total energy absorption. The 4-layer laminates provided the most balanced performance between structural strength, deformation capability, and energy absorption. Among all specimens, CC$[45/-45]_4$ showed the highest energy absorption and specific energy absorption, with values of 0.145 kJ and 0.364 kJ/kg, respectively. Among the hybrid laminates, CG$[45/-45]_4$ provided performance close to that of the full carbon fiber laminate while reducing material cost, demonstrating its potential for lightweight automotive impact structures.

The finite element analysis showed good agreement with the experimental results in terms of deformation patterns, collapse modes, and absorbed energy. The numerical model successfully captured the main damage mechanisms observed during impact, including laminar buckling, fiber buckling, transverse cracking, and corner damage. The results also confirmed that reducing laminate thickness to fewer than four layers significantly decreased structural resistance and energy absorption capability.

Overall, hybrid double hat structures with a [45/−45] fiber orientation and moderate laminate thickness provide an effective balance between strength, deformation capability, energy absorption, and material cost. These findings offer useful guidance for designing lightweight impact-resistant composite structures for automotive applications. However, the material properties used in the numerical simulations were adopted from published literature rather than experimentally measured in this study. Future work should include experimental material characterization, sensitivity analysis, and additional hybrid laminate configurations to improve the predictive accuracy and practical applicability of the numerical model.

Acknowledgments

The researchers also wish to extend their appreciation to The Material's Impact Resistance Testing Research Unit (Mat-Pact Unit), Faculty of Industry and Technology, Rajamangala University of Technology Isan Sakon Nakhon Campus, for providing equipment support for this research endeavor.

Author Contributions

W. Senakum and K. Sakkampang planned the scheme, initiated the project, and suggested the experiments; W. Senakum, K. Sakkampang and N. Onsalung conducted the experiments and analyzed the empirical results; W. Senakum, K. Sakkampang and N. Onsalung developed the mathematical modeling and examined the theory validation. The manuscript was written through the contribution of all authors. All authors discussed the results, reviewed, and approved the final version of the manuscript.

Conflicts of Interest

The authors declare no conflict of interest.

Declaration of generative AI and AI-assisted technologies in the writing process

The authors utilized the ChatGPT tool to enhance the language and readability of the manuscript.

References

[1] X. Song, G. Sun, and Q. Li, "Sensitivity analysis and reliability based design optimization for high-strength steel tailor welded thin-walled structures under crashworthiness," *Thin-Walled Structures*, vol. 109, pp. 132-142, Dec. 2016, doi: 10.1016/j. tws. 2016.09.003.

[2] H. N. Han and J. P. Clark, "Lifetime costing of the body-in-white: Steel vs aluminum," *The Journal of The Minerals, Metals & Materials Society (TMS)*, vol. 47, pp. 22–28, 1995, doi: 10.1007/BF032 21171.

[3] X. T. Cui, S. X. Wang, and S. J. Hu, "A method for optimal design of automotive body assembly using mutli-material construction," *Materials & Design*, vol. 29, no. 2, pp. 381-387, Feb. 2008, doi: 10.1016/j.matdes.2007.01.024.

[4] A. Keshavarzi and H. S. Googarchin, "Local reinforcement of adhesively bonded square shape aluminum energy absorber with CFRP under quasi-static axial loading: An experimental and numerical study," *International Journal of Adhesion and Adhesives*, vol. 135, Art. no. 103823, Oct. 2024, doi: 10.1016/j.ijadhadh.2024.103823.

[5] J. Obradovic, S. Boria and B. Belingardi, "Lightweight design and crash analysis of composite frontal impact energy absorbing structures," *Composite Structures*, vol. 94, no. 2, pp. 423-430, Jan. 2012, doi: 10.1016/j. compstruct. 2011.08.005.

[6] M. Mani, "Silica nanoparticle-enhanced mechanical properties and energy absorption behavior of hybrid fiber-reinforced polymer composites for structural applications," *Next Materials*, vol. 9, Art. no. 101213, Aug. 2025, doi: 10.1016/j.nxmate.2025.101213.

[7] S. Ekşi, L. Salman, M. F. Beşiroğlu, and M. Memişoğlu, "Open hole strength and damage behavior of GFRP and CFRP composites," *Engineering Failure Analysis*, vol. 176, Art. no. 109584, Nov. 2025, doi: 10.1016/j.engfailanal. 2025.109584.

[8] Y. Li, H. Qin, L. Jia, T. E. Tay, V. B. C. Tan, and Y. Liu, "Microstructure dependent transverse strength criterion for UD-CFRP composites via computational micromechanics and machine learning," *Composites Science and Technology*, vol. 251, Art. no. 110551, May 2024, doi: 10.1016/j.compscitech.2024.110551.

[9] Y. Zhou, M. Wang, Y. Lian, N. Yang, Y. Liu, and M. Zeng, "Fatigue and corrosion interaction: Performance evolution mechanisms in reinforced concrete beams strengthened with CFRP anchorage system," *Construction and Building Materials*, vol. 496, Art. no. 143784, Nov. 2025, doi: 10.1016/j.conbuildmat.2025. 143784.

[10] M. Mund, K. Lippky, D. Blass, and K. Dilger, "Influence of production based surface topography and release agent amount on bonding properties of CFRP," *Composite Structures*, vol. 216, pp. 104–111, May 2019, doi: 10.1016/j.compstruct.2019. 02.026.

[11] J. Ge, G. Fu, J. H. S. Almeida Jr., Y. Jin, and D. Sun, "Thermal effect in CFRP machining: Temperature field characteristics, heat generation mechanism and thermal damage management," *Composite Structures*, vol. 356, Art. no. 118845, Jan. 2025, doi: 10.1016/j. compstruct.2025.118845.

[12] Y. Tong et al., "An organic-inorganic interface structure for CFRP and the enhancement of mechanical properties at room/high temperature," *Composites Part B: Engineering*, vol. 291, Art. no. 112009, Feb. 2025, doi: 10.1016/j.com positesb.2024.112 009.

[13] O. K. Meyer et al., "Multichannel hollow carbon fiber reinforcement in an epoxy resin matrix for direct ink writing of high-performance composites," *Materials & Design*, vol. 259, Art. no. 114744, Nov. 2025, doi: 10.1016/j.matdes. 2025.114744.

[14] B. Sun and J. Yu, "High-performance composites and their applications," in *Porous Lightweight Composites Reinforced With Fibrous Structures*, Y. Yang, J. Yu, H. Xu, and B. Sun, Eds. Berlin, Germany: Springer, 2017, ch. 13, pp. 297–324, doi: 10.1007/978-3-662-53804-3_13.

[15] M. Jatulis, E. Elghandour, and N. Elzayady, "Evaluation of the mechanical properties of aircraft composite materials after

indentation," *Journal of Mechanical Science and Technology*, vol. 37, no. 11, pp. 5813–5821, Nov. 2023, doi: 10.1007/s1220 6-023-1020-6.
[16] R. Y. Tang, Y. L. Sun, Y. G. Wang, R. Ding, J. S. Fan, and J. G. Nie, "Finite element analysis of single steel-plate concrete composite containment of nuclear power plant under commercial aircraft impact", *Engineering Structures*, vol. 321, Art. no. 118998, Dec. 2024, doi: 10.1016/j.engstruct.2024.118998.
[17] E. S. Elumalai, R. Asokan, S. Pragadheswaran, T. Sivagangai, R. Sateesh, and S. Seralathan, "Impact analysis on an integrated carbon composite wing spar of fixed wing aircraft," *Materials Today: Proceedings*, 2023, doi: 10.1016/j.matpr.2023.04.250.
[18] S. J. Arunachalam, S. Thanikodi, and R. Saravanan, "Effect of nano-hybridization on flexural and impact behavior of jute/kenaf/glass fiber-epoxy composites for automotive application," *Results in Engineering*, vol. 25, Art. no. 104571, Mar. 2025, doi: 10.1016/j. rineng.2025.104571.
[19] M. S. U. Abrar, K. F. N. Ezaz, M. J. Hasan, R. I. Pranto, T. A. Alvy, and M. Z. Hossain, "Speed-dependent impact analysis on a car bumper structure using various materials," *Results in Engineering*, vol. 21, Art. no. 101927, Mar. 2024, doi: 10.1016/j.rineng.2024.101927.
[20] H. Hazari, K. S. Kumar, and A. C. Reddy, "Crashworthiness and explicit dynamic analysis of a car body structure with different materials in multi-obstacle collision," *Progress in Engineering Science*, vol. 2, no. 4, Art. no. 100133, Dec. 2025, doi: 10.1016/j.pes. 2025. 100133.
[21] M. Rodríguez-Marcos, P. Villanueva-Llaurado, J. Fernández-Gómez, and J. López-Rebollo, "Effectiveness of coated carbon fibre cementitious matrix systems for flexural strengthening of concrete beams," *Engineering Structures*, vol. 325, Art. no. 119443, Feb. 2025, doi: 10.1016/j.eng struct.2024.119443.
[22] Z. Qiu, M. Li, G. Li, X. Li, and Y. Wang, "Testing, simulation, and design of square concrete-filled steel tubular beam-columns with internal I-section carbon fiber-reinforced polymer profiles under cyclic loading," *Engineering Structures*, vol. 341, Art. no. 120819, Oct. 2025, doi: 10.1016/j.eng struct.20 25.120819.
[23] E. Kosedag and R. Ekici, "Low-velocity impact behaviors of B4C/SiC hybrid ceramic reinforced Al6061 based composites: An experimental and numerical study," J*ournal of Alloys and Compounds*, vol. 1010, Art. no. 177525, Jan. 2025, doi: 10.1016/j.jallcom.2024.177525.
[24] P. V. Trinh, J. Lee, B. Kang, P. N. Minh, D. D. Phuong, and S. H. Hong, "Mechanical and wear properties of SiCp/CNT/Al6061 hybrid metal matrix composites," *Diamond and Related Materials*, vol. 124, Art. no. 108952, Apr. 2022, doi: 10.1016/j.diamond.2022.108952.
[25] E. Kosedag, M. Aydin, and R. Ekici, "Effect of stacking sequence and metal volume fraction on the ballistic impact behaviors of ARALL fiber-metal laminates: an experimental study," *Polymer Composites*, vol. 43, no. 3, pp. 1536–1545, Mar. 2022, doi: 10.1002/pc.26474.
[26] Z. Zhang, Q. Liu, J. Fu, and Y. Lu, "Parametric study on the crashworthiness of the Al/CFRP/GFRP hybrid tubes under quasi-static crushing," *Thin-Walled Structures*, vol. 192, Art. no. 111156, Nov. 2023, doi: 10.1016/j.tws.2023 .111156.
[27] G. Zhu, G. Sun, H. Yu, S. Li, andQ. Li, "Energy absorption of metal, composite and metal/composite hybrid structures under oblique crushing loading," *International Journal of Mechanical Sciences*, vol. 135, pp. 458–483, Jan. 2018, doi: 10.1016/j.ijmecsci.2017.11.017.
[28] Y. F. Su, X. M. Ge, X. C. Zhang, C. Chen, L. H. Ma, and W. Zhou, "Damage behavior of composite/metal hybrid tubes under low-velocity impact: A deep learning and mode decomposition-based acoustic emission approach," *Thin-Walled Structures*, vol. 214, Art. no. 113428, Sep. 2025, doi: 10.1016/j.tws.2025.113428.
[29] N. Nawawithan, P. Kittisakpairach, S. Nithiboonyapun, K. Ruangjirakit, and P. Jongpradist, "Design and performance simulation of hybrid hemp/glass fiber composites for automotive front bumper beams," *Composite Structures*, vol. 335, Art.

no. 118003, May 2024, doi: 10.1016/j.compstruct .2024.118003.
[30] H. Golivari, H. S. Googarchin, A. Zaeri, and A. Keshavarzi, "Experimental and numerical investigation of the energy absorption in hybrid double-hat thin-walled structures reinforced by adhesive bonding under three-point bending," *International Journal of Adhesion and Adhesives*, vol. 128, Art. no. 103543, Jan. 2024, doi: 10.1016/j.ijadhadh. 2023.103543.
[31] N. Fantuzzi, M. Bacciocchi, D. Benedetti, and J. Agnelli, "The use of sustainable composites for the manufacturing of electric cars," *Composites Part C: Open Access*, vol. 4, Art. no. 100096, Mar. 2021, doi: 10.1016/j.jcomc.2020.100096.
[32] X. Miao et al., "Design of novel sandwich double-hat beams filled with aluminum hierarchical structures under axial impact loading," *Structures*, vol. 70, Art. no. 107758, Dec. 2024, doi: 10.101 6/j.istruc.2024.107758.
[33] C. Qi, Y. Sun, and S. Yang, "A comparative study on empty and foam-filled hybrid material double-hat beams under lateral impact," *Thin-Walled Structures*, vol. 129, pp. 327–341, Aug. 2018, doi: 10.1016/j.tws.2018.04.015.
[34] C. Qi, Y. Sun, H. T. Hu, D. Z. Wang, G. J. Cao, and S. Yang, "On design of hybrid material double-hat thin-walled beams under lateral impact," *International Journal of Mechanical Sciences*, vol. 118, pp. 21–35, Nov. 2016, doi: 10.1016/j.ijmecsci.2016.09. 008.
[35] K. Sato, T. Inazumi, A. Yoshitake and S. D. Liu, "Effect of material properties of advanced high strength steels on bending crash performance of hat-shaped structure," *International Journal of Impact Engineering*, vol. 54, pp. 1–10, Apr. 2013, doi: 10.1016/j.ijimpeng.2012.10.012.
[36] S. F. Abdulqadir and T. Tarlochan, "Composite Hat Structure Design for Vehicle Safety: Potential Application to B-Pillar and Door Intrusion Beam," *Materials*, vol. 15, no. 3, Art. no. 1084, Feb. 2022, doi: 10.3390/ma15031084.
[37] D. Chen, G. Sun, X. Jin, and Q. Li, "Quasi-static bending and transverse crushing behaviors for hat-shaped composite tubes made of CFRP, GFRP and their hybrid structures," *Composite Structures*, vvol. 239, Art. no. 111842, May 2020, doi: 10.1016/j.compstruct.2019.111842.
[38] J. Bidadi, H. H. Miandowab, H. S. Googarchin, A. Akhavan-Safar, and L. F. M. da Silva, "Experimental and numerical investigation on the crashworthiness performance of double hat-section Al-CFRP beam subjected to quasi-static bending test," *Polymer Composites*, vol. 45, no. 6, pp. 5656–5674, Jun. 2024, doi: 10.1002/pc. 28155.
[39] A. Saber, A. M. Amer, A. Abd_Elsalam, A. I. Shehata, and H. A. El-Gamal, "Design and optimization of a bio-inspired crash box based on seashell structure for enhanced crashworthiness," *Results in Engineering*, vol. 32, Art. no. 111724, Dec. 2026, doi: 10.10 16/j.rineng.2026.111724.
[40] T. Fischer et al., "Experimental and numerical investigations on the quasi-static structural properties of fibre metal laminates processed by thermoforming," *Composite Structures*, vol. 258, Art. no. 113418, Feb. 2021, doi: 10.1016/j.comp struct.2020.113418.
[41] M. Dai, L. Ying, S. Wang, H. Ma, P. Hu and Y. Wang, "Modeling the crashworthiness analysis of functional graded strength thin-walled structure with phenomenological GISSMO model," *Thin-Walled Structures*, vol. 180, Art. no. 109766, Nov. 2022, doi: 10.1016/j.tws.2022.109766.
[42] N. Qiu, Y. Gao, J. Fang, Z. Feng, G. Sun, and Q. Li, "Theoretical prediction and optimization of multi-cell hexagonal tubes under axial crashing", *Thin-Walled Structures*, vol. 102, pp. 111–121, May 2016, doi: 10.1016/j.tws.2016. 01.023.
[43] H. Jiang, and Y. Ren, "Crashworthiness and failure analysis of steeple-triggered hat-shaped composite structure under the axial and oblique crushing load", *Composite Structures*, vol. 229, Art. no. 111375, Dec. 2019, doi: 10.1016/j. compstruct.201 9.111375.
[44] M. Jawaid, H. P. S. Abdul Khalil, and A. Abu Bakar, "Woven hybrid composites: Tensile and flexural properties of oil palm-woven jute fibres based epoxy composites," *Materials Science and Engineering: A*, vol.

528, no. 15, pp. 5190–5195, Jun. 2011, doi: 10.1016/j.msea.2011.03.047.

[45] Y. Liu, T. Zhao, W. Ju, and S. Shi, "Materials discovery and design using machine learning," *Journal of Materiomics*, vol. 3, no. 3, pp. 159–177, Sep. 2017, doi: 10.1016/j.jmat.2017. 08.002.

[46] S. Ghosh, K. Lee, and S. Moorthy, "Multiple scale analysis of heterogeneous elastic structures using homogenization theory and voronoi cell finit element method," *International Journal of Solids and Structures*, vol. 32, no. 1, pp. 27–62, Jan. 1995, doi: 10.1016/0020-7683(94)00097-G

[47] L. Techawinyutham, V. Ayyappan, M. Kumar, V. Raghunathan, S. M. Rangappa, and S. Siengchin, "Sustainable epoxy composites from hemp/pineapple/glass fibers for lightweight automobile panels," *International Journal of Biological Macromolecules*, vol. 337, pt. 1, Art. no. 149392, 2026, doi: 10.1016/j.ijbiomac. 2025. 14 9392.

[48] M. Kumar, G. Vashishtha, B. Dhiman, and S. Chauhan, "Bearing response prediction in hydrothermal aged carbon fiber reinforced epoxy composite joints using machine learning techniques," *Mechanics of Advanced Composite Structures*, vol. 12, Special Issue 2, pp. 329–338, 2025, doi: 10.22075/macs.202 4.33802.1643.

[49] A. Y. Chen, S. Baehr, A. Turner, Z. Zhang, and G. X. Gu, "Carbon-fiber reinforced polymer composites: A comparison of manufacturing methods on mechanical properties," *International Journal of Lightweight Materials and Manufacture*, vol. 4, no. 4, pp. 468–479, Dec. 2021, doi: 10.10 16/j.ijlmm.2021.04.001.

[50] M. Kumar and J. Saini, "Computational analysis of bidirectional carbon fibre/epoxy nanocomposites using different failure criteria," *Proceedings of the Institution of Mechanical Engineers*, Part E: Journal of Process Mechanical Engineering, vol. 237, no. 4, pp. 1286–1299, Aug. 2023, doi: 10.117 7/095440 89 221112375.

[51] Y. Zhao and X. Zhou, "Numerical analysis of unidirectional carbon-fibre/epoxy composite laminates under low velocity impacts of different forms," *Computational Materials Science*, vol. 231, Art. no. 112611, Jan. 2024, doi: 10.1016/j. commatsci.2023.112611.

[52] Z. Ying, J. Li, Z. Xiang, X. Hu, and Z. Wu, "Impact damage characteristics of braided/unidirectional hybridization laminates when impacted on different sides," *International Journal of Impact Engineering*, vol. 172, Art. no. 104396, Feb. 2023, doi: 10.1016/j.ijimpeng. 2022.104396.

[53] M. T. Aranda and D. Leguillon, "Prediction of failure of hybrid composites with ultra-thin carbon/epoxy layers using the Coupled Criterion," *Engineering Fracture Mechanics*, vol. 281, Art. no. 109053, Mar. 2023, doi: 10.1016/j.engfracmech.2023.109 053.

[54] J. Ye et al., "Microscale intrinsic properties of hybrid unidirectional/woven composite laminates: Part I experimental tests," *Composite Structures*, vol. 262, Art. no. 113369, Apr. 2021, doi: 10.1016/ j.compstruct.2020. 113369.

[55] Y. Ji, Z. Gao, W. Chen, H. Huang, M. Li, and X. Li, "Study on the deformation mode and energy absorption characteristics of a corner-enhanced biomimetic spider web hierarchical structure," *Thin-Walled Structures*, vol. 199, Art. no. 111810, 2024, doi: 10.1016/j.tws.202 4.111810.

[56] Z. Han et al., "Simultaneous enhancements of energy absorption and strength driven by hexagonal close-packed lattice structures of resin revealed by in-situ compression," *Thin-Walled Structures*, vol. 197, Art. no. 111586, Apr. 2024, doi: 10.1016/j.tws.2024.111586.

[57] H. Gharehbaghi and A. Farrokhabadi, "Experimental, analytical, and numerical studies of the energy absorption capacity of bi-material lattice structures based on quadrilateral bipyramid unit cell," *Composite Structures*, vol. 337, Art. no. 118042, Jun. 2024, doi: 10.1016/j.compstruct.2024.118042.

[58] K. Sakkampang and N. Onsalung, "Energy absorption capacity of rubber sponge reinforcement in carbon fiber reinforced plastics (CFRP) tubes," I*nternational Journal of Crashworthiness*, vol. 28, no. 4, pp. 484–497, 2023, doi: 10.1080/13588265.2022. 2109670.

[59] S. Palanivelu, W. Van Paepegem, J. Degrieck, and D. Kakogiannis, "Comparative study of the quasi-static

energy absorption of composite tubes," *Polymer Testing*, vol. 29, no. 3, pp. 381–396, Apr. 2010, doi: 10.1016/j.polymertesting. 2010.01.003.

[60] A. G. Mamalis, D. E. Manolakos, G. A. Demosthenous, and M. B. Ioannidis, "Crashworthiness of Composite Thin-Walled Structures," *Taylor & Francis, London*, 1998.

[61] G. Reyes V. and W. J. Cantwell, "The mechanical properties of fibre-metal laminates based on glass fibre reinforced polypropylene," *Composites Science and Technology*, vol. 60, no. 7, pp. 1085–1094, Jun. 2000, doi: 10.1016/S0266-3538 (00)00 002-6.

[62] X. Deng, J. Hu, W.-X. Wang, and T. Matsubara, "A micromechanical model for the analysis of multidirectional fiber reinforced polymer laminates," *Composite Structures*, vol. 208, pp. 507–516, Jan. 2019, doi: 10.101 6/j.compstruct. 2018.10.019.

[63] A. A. A. Alghamdi, "Collapsible impact energy absorbers: An overview," *Thin-Walled Structures*, vol. 39, no. 2, pp. 189–213, Feb. 2001, doi: 10.1016/S0263-8231(00)00048-3.

[64] P. T. Goncalves, A. Arteiro, N. Rocha, and F. Otero, "Coupled longitudinal and transverse damage modeling of fiber-reinforced polymers using a smeared crack approach," *International Journal of Solids and Structures*, vol. 311, Art. no. 113252, Mar. 2025, doi: 10.1016/j.ijsolstr. 2025. 113252.

[65] G. R. Ibrahim, A. Albarbar, and K. F. Brethee, "Damage degradation modelling for transverse cracking in composite laminates under low-velocity impact," *Engineering Fracture Mechanics*, vol. 263, Art. no. 108286, Mar. 2022, doi: 10.1016/j.engfrac mech.2022.108286.